Journal of
Composites Science

MDPI

Article

Synthesis and Characterization of Titanium and Vanadium Nitride–Carbon Composites

Helia M. Morales [1,2], David A. Sanchez [3], Elizabeth M. Fletes [3], Michael Odlyzko [4], Victoria Padilla-Gainza [3], Mataz Alcoutlabi [3] and Jason G. Parsons [5,*]

1 School of Integrative Biological and Chemical Sciences, University of Texas Rio Grande Valley, 1 West University Blvd., Brownsville, TX 78521, USA; helia.morales@utrgv.edu
2 Escuela de Ingeniería y Ciencias, Tecnológico de Monterrey, Av E. Garza Sada 2501, Monterrey 64700, NL, Mexico
3 Department of Mechanical Engineering, University of Texas Rio Grande Valley, 1201 West University Dr., Edinburg, TX 78539, USA; david.sanchez11@utrgv.edu (D.A.S.); elizabeth.fletes01@utrgv.edu (E.M.F.); victoria.padilla@utrgv.edu (V.P.-G.); mataz.alcoutlabi@utrgv.edu (M.A.)
4 Characterization Facility, College of Science and Engineering, 55 Shepherd Laboratories, University of Minnesota, Minnesota, MN 55455-0431, USA; odlyz003@umn.edu
5 School of Earth Environmental and Marine Sciences, University of Texas Rio Grande Valley, School 1 West University Blvd., Brownsville, TX 78521, USA
* Correspondence: jason.parsons@utrgv.edu; Tel.: +1-(956)-882-7772

Abstract: Titanium nitride and vanadium nitride–carbon-based composite systems, TiN/C and VN/C, were prepared using a new synthesis method based on the thermal decomposition of titanyl tetraphenyl porphyrin (TiOTPP) and vanadyl tetraphenyl porphyrin (VOTPP), respectively. The structure of the TiN/C and VN/C composite materials, as well as their precursors, were characterized using Fourier Transformed Infrared Spectroscopy, X-Ray diffraction (XRD), X-Ray energy dispersive (EDS) and X-Ray photoelectron spectroscopy (XPS). Morphologies of the TiN/C and VN/C composites were examined by means of scanning electron (SEM) and transmission electron (TEM) microscopy. The synthesis of the non-metalated tetraphenyl porphyrin, the titanium, and vanadium tetraphenyl porphyrin complexes were confirmed using FTIR. The thermal decomposition of the titanium and vanadium tetraphenyl porphyrin complexes produced the respective metal nitride encapsulated in a carbon matrix; this was confirmed by XRD, SEM, TEM, and XPS. From the XRD patterns, it was determined that the TiN and VN were presented in cubic form with expected space group FM-3M and 1:1 (metal:N) stoichiometry. The XPS results confirmed the presence of both TiN and VN in the carbon matrix without metal carbides. The SEM and TEM results showed that both TiN and VN nanoparticles formed small clusters throughout the carbon matrix; the EDS results revealed a uniform composition. The synthesis method presented in this work is novel and serves as an effective means to produce TiN and VN NPs with good structure and morphology embedded in a carbon matrix.

Keywords: thermal decomposition; TiOTPP; VOTPP; TiN–C; VN–C; metal nitride carbon composite

Citation: Morales, H.M.; Sanchez, D.A.; Fletes, E.M.; Odlyzko, M.; Padilla-Gainza, V.; Alcoutlabi, M.; Parsons, J.G. Synthesis and Characterization of Titanium and Vanadium Nitride–Carbon Composites. *J. Compos. Sci.* **2024**, *8*, 485. https://doi.org/10.3390/jcs8120485

Academic Editor: Chun-Liang Yeh

Received: 24 October 2024
Revised: 18 November 2024
Accepted: 20 November 2024
Published: 21 November 2024

1. Introduction

The current economic growth of societies requires the development, processing, and production of electrode materials for energy storage. Typically, energy is stored using electrochemical energy storage (EES) devices such as batteries and capacitors/supercapacitors. Within these technologies, electrode materials are the key components determining the utility of EES devices. The electrochemical performance of the electrode material can be improved by increasing its energy density, specific power, reversibility, transport rates, and cycle life [1,2]. In the last few years, different electrode materials were synthesized to improve the electrochemical performance of lithium-ion batteries (LIBs), such as transition

metal oxides (TMOs), carbides (TMCs), nitrides (TMNs), metal sulfides (MSs), phosphides (TMPs), and carbon-based composite materials [3–5]. Transition metal nitrides have attracted a lot of attention due to their high chemical and thermal stability, high melting points, hardness, and electrical conductivity [1,3,6]. Thus, TMNs are considered promising electrode materials for LIBs, lithium–sulfur batteries, and supercapacitors [1,7]. In addition to energy storage, TMNs have been used in water-splitting devices, catalytic dye degradation systems, fuel cells, CO_2 reduction products, dye-synthesized solar cells, and biosensors [8–10]. TMNs have been engineered to overcome their pulverization and air instability by reducing active materials to nanoscale dimensions and developing customized nanostructures with desired properties [11,12]. Carbon-based materials show promise for use in electrochemical devices [13]. Metal nitrides embedded in a carbon matrix, such as mesoporous carbon, carbon fibers, carbon nanosheets, graphitic carbon, hard carbon, graphene, carbon nanocubes, or carbon nanotubes have been widely used to improve the electrical/ionic conductivity and reduce the volume change in active materials in LIBs [14,15]. The improved electrochemical performance of TMNs/carbon nanocomposites has been attributed to their high surface area to volume ratio and electrical conductivity, as well as high ionic diffusivity at the electrolyte–electrode interface [14,16,17]. Metal nitrides such as TiN, VN, GaN, MnN, NiN, MoN, FeN, and Ni_3N have been used to prepare carbon-based composites for EES devices [7,10,18]. Both TiN and VN exhibit promising properties for electrochemical applications when embedded in carbon [19]. Several systems of TiN/C and VN/C composites based on hard carbon [20–23], graphene [9,19,24–29], nanosheets [30–34], and nanotubes [35–37] were synthesized and used as composite electrode materials for EES devices.

Morales et al. [16,17] synthesized nanocomposites of amorphous carbon and metal nitride through the thermal decomposition of a metal-substituted phthalocyanine. The method proved to be fast and efficient and had the advantage of using common, long shelf-life precursors. The resultant nanocomposites were used as anode materials for LIBs. The TiN/C composite electrode showed a specific capacity of 320 mAg^{-1} after 100 cycles at a current density of 100 mAg^{-1}, while the VN/C composite delivered a specific capacity of 307 mAh g^{-1} after 100 cycles and Coulombic efficiency of 99.8 at the 100th cycle. In the present work, TiN/C and VN/C nanocomposites were prepared by a new synthesis method based on the thermal decomposition of titanium tetraphenyl porphyrin (TiOTPP) and vanadium tetraphenyl porphyrin (VOTPP), respectively. The tetraphenyl porphyrin was synthesized via a condensation reaction and was metal substituted using titanium tetrachloride ($TiCl_4$) or vanadyl acetylacetonate ($VO(C_5H_7O_2)_2$). The non-metaled and metalated TPPs were thermally decomposed by heating the samples in a tube furnace under nitrogen at 750 °C for 5 h. The decomposition resulted in the formation of non-graphitic carbon TiN/C and VN/C nanocomposites. The structure, chemical composition, and morphology of the precursors and the TiN/C and VN/C nanocomposites were characterized using XRD, FTIR, SEM, TEM, EDS, and XPS.

2. Methods

2.1. Material Synthesis

Analytical-grade reagents were used without further purification unless specified explicitly in the procedure. TiOTPP and VOTPP were prepared using a two-step process. First, a non-metalated porphyrin was synthesized (H_2TPP), which was subsequently metalated using Ti or V. Complexes were prepared using modified versions of existing methods [38,39]. Freshly distilled pyrrole was added to benzaldehyde in propionic acid at a molar ratio of 1:1, and then the solution was refluxed for three hours. The solvent (propionic acid) was removed by evaporation under reduced pressure, while the remaining solid was washed several times using methanol and dried. The metalation with Ti or V was performed by mixing either $TiCl_4$ or $(VO(C_5H_7O_2)_2$ with H_2TPP with an 8:1 molar ratio in 1-chloronaphthalene and refluxed for 4 h. Subsequent to the reaction, the solvent was removed by evaporation under reduced pressure. The remaining solid was extracted

using water-saturated dichloromethane (DCM), and the DCM layer was saved. The DCM phase was added to a neutral alumina column and eluted using a mixture of DCM/hexane (99:1 v/v). Once the sample was eluted, the metalated TPPs were recovered by solvent evaporation under reduced pressure. The TiN/C and VN/C composites were prepared by heating the metalated TPP in a Thermolyne horizontal tube furnace (model F79330-33-70, Thermo Fisher Scientific, Waltham, MA, USA). The quartz tube was purged with UHP nitrogen for 15 min, and the temperature was increased from room temperature to 750 °C at a rate of 10 °C min^{-1}. The final temperature of 750 °C was maintained for 5 h under a constant nitrogen flow. After the reaction, the sample was cooled to room temperature naturally under a constant nitrogen flow.

2.2. Characterization

The synthesized compounds were dried and finely ground using a mortar and pestle, followed by characterization using FTIR, XRD, SEM, EDS, TEM, and XPS. The FTIR spectra of the products were collected using a Perkin–Elmer Frontier FTIR spectrometer using the attenuated total reflection (ATR) accessory. The range of the spectra was 4000–650 cm^{-1}; then 32 scans of each sample were collected at a resolution of 4 cm^{-1}. The data were analyzed using Spectrum software (Version 8.0, Perkin Elmer, Waltham, MA, USA).

The powder XRD patterns were collected using a Bruker D2 Phaser powder diffractometer with a cobalt source (K_α = 1.789 Å) and an iron filter. The diffraction patterns were collected over the range of 10 to 80° in 2θ with a 0.05° step size and 5 s counting time. The diffraction patterns were fitted using the Le Bail fitting procedure using the FullProf Suite software (Version 5.10) and crystallographic data reported in the literature [16,17,40–46]. The morphology of the products were examined using SEM; the images were collected using a Sigma VP Carl Zeiss scanning electron microscope (Carl Zeiss, White Plaines, NY, USA) operated with accelerated voltages between 2.0 and 6.0 kV at a working distance of up to 6.5 mm. Energy Dispersive Spectroscopy (EDS) (EDAX, Mahwah, NJ, USA) was used to analyze the elemental composition of the samples. Elemental mapping and EDS spectra analysis were used to analyze the distribution of C, O, N, and V, or Ti elements in the samples. TEM images were collected using FEI Titan G2 60-300 and Thermo Fisher Talos F200X microscopes (Thermo Fisher Scientific, Waltham, MA, USA), operated with an accelerating voltage of 200 kV. The XPS spectra were collected using a Thermo Scientific K-Alpha Photoelectron Spectrometer (Thermo Fisher Scientific, Waltham, MA, USA) using a micro-fused monochromatic Al K-α (1486.7 eV) source with scans at 0.1 eV and a spot size of 400 μm and analyzed using the CASA XPS software (Version 2.3.25, Casa Software Limited, Teignmouth, UK) [47].

3. Results

3.1. FTIR

The FTIR spectra collected for the H_2TPP, TiOTPP, and VOTPP are shown in Figure 1. The main IR absorption bands and assignments are presented in Table 1. The results coincide with those reported on similar structures, which present the characteristic bands and confirm the synthesis of the free-based and metalated compounds. The observed bands in the high wavenumber region correspond to N–H stretching bands and stretching vibrational motion of C–H bonds of the porphyrin ring [48]. The mid-wavenumber exhibits the porphyrin skeletal, C–C pyrrole stretching, and N–H deformation modes [48]. The bands at 1487 cm^{-1} to 1595 cm^{-1} are associated with C–C and C=C stretching modes, respectively [49–51]. Bands observed in the low wavenumber region correspond to in-plane bending, out-of-plane bending, ring rotation, and torsion modes of porphyrin skeletal. Additionally, the bands located in the 650–750 cm^{-1} range arise from bending and vibration of the phenyl groups [48]. The free-based H_2TPP presents the N–H bond stretching and bending located at 3308 cm^{-1} (in-plane) and 965 cm^{-1} (out-of-plane); after the metalation, the two hydrogens were substituted by the metal ion while the two bands were not present in either the TiOTPP or VOTPP [51]. The stretches observed in the 1350 cm^{-1} range

correspond to the C=N stretching and were observed to shift from 1341 cm^{-1} to 1359 and 1367 cm^{-1} in the Ti=O and V=O TPP samples, respectively, indicating the coordination of the metal ions to the nitrogen atoms and confirming the metalation of the free-based H_2TPP. The strong band located near 1000 cm^{-1} also corresponds to the skeletal ring vibration of the metal-substituted porphyrin [51]. The bands at 804 cm^{-1} and 963 cm^{-1} indicated the presence of Ti=O and V=O in the respective metalated products [52,53].

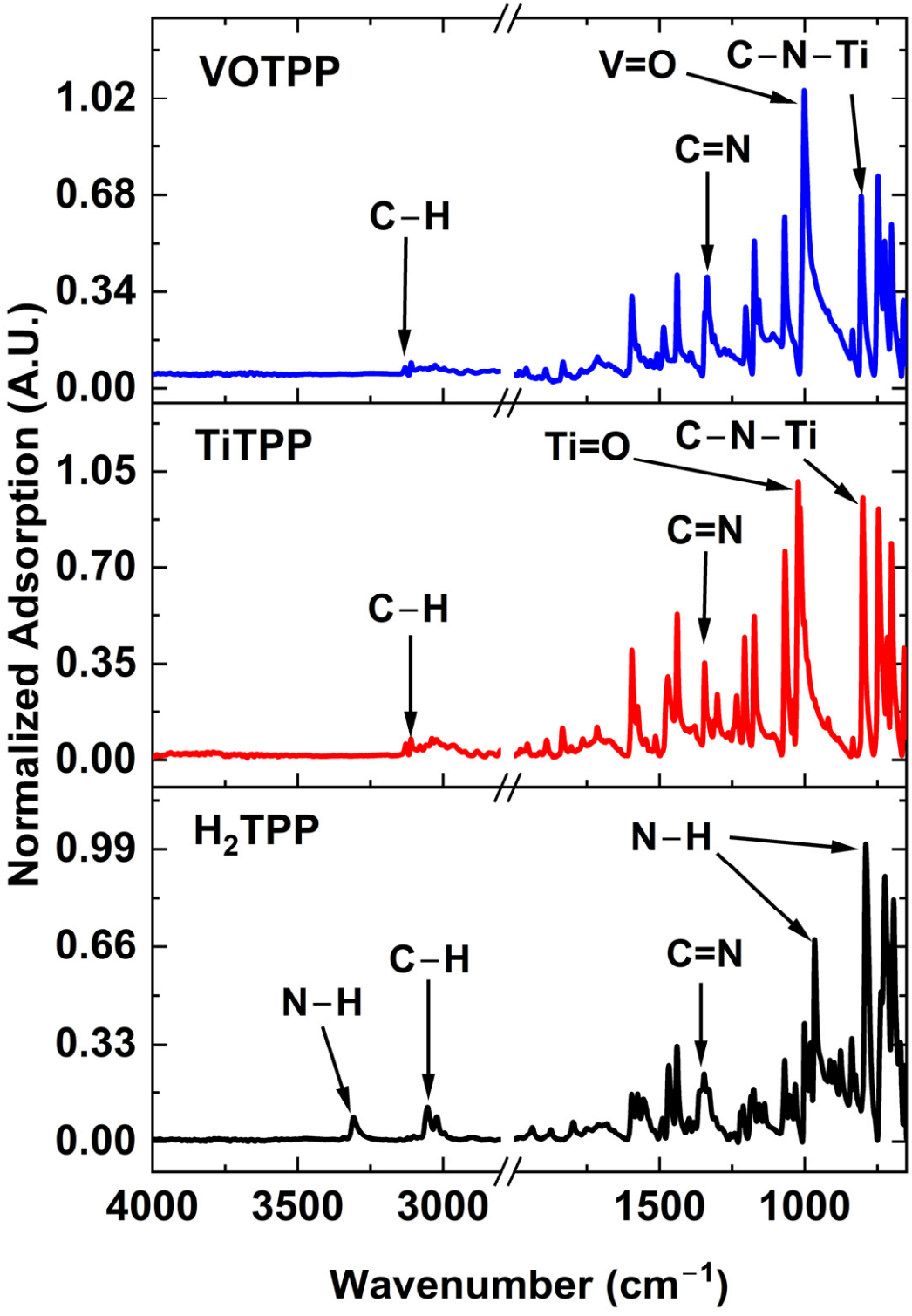

Figure 1. FTIR spectra of H_2TPP (**bottom**), TiOTPP (**middle**), and VOTPP (**top**).

Table 1. FTIR bands position and assignments for the H_2TPP, TiOTPP, and VOTPP.

H_2TPP Band Position (cm^{-1})	TiOTPP Band Position (cm^{-1})	VOTPP Band Position (cm^{-1})	Assignment
656	658	656	C–H bending ring [49,54]
670			C–H bending of phenyl [49,54]
694	701	701	C–H bending of phenyl [54,55]
724	724	724	C–H out-of-plane vibration [49]
	747	750	Pyridine fold and phenyl ring [48]
790			N–H out of plane bending vibration [49]
	804	807	
826			
838	836	883	In-plane distortion of pyrrole ring [49]
877	882	881	N–H stretching coupling with isoindole deformation [52]
900			Aromatic ring deformation [56]
913	919	923	Phenyl ring [48]
	963	967	Ti=O stretching [52,53]. V=O stretching [16,57]
965			N–H vibration in pyrrole ring [51,58,59]
980			Stretching vibrations of pyrrole rings [48]
1001	1001	1006	Stretching vibrations of pyrrole rings [55] and skeletal ring vibration of metal porphyrin [51,59–61]
1033	1035	1038	C–H plane bending vibrations in benzene [62]
1053			C–H plane bending vibrations in benzene [62]
1069	1068	1070	C–N stretching vibrations in pyrrole and C-H bending of phenyl rings [55,58]
1138			Phenyl ring [48]
1158	1158	1159	C–H in phenyl [63]
1175	1173	1174	C–H bending vibrations [49]
1211	1200	1203	C=N [63]
1335	1334	1336	C=N stretching vibrations in pyrrole [49,51,64]
1341			C=N stretching vibrations in pyrrole [49,51,64]
	1359	1367	C–N stretching vibration of metal-substituted porphyrin ring [65]
1398			C–H stretching vibration [62]
1440	1440	1438	Benzene vibration [58]
1468			Benzene vibration [58]
1489	1487	1486	C–C stretching vibration [49]
1556			C=C stretching vibration [51]
1575			C–C stretching vibration [49]
1596	1595	1595	C–C stretching in ring [50]
3022	3025	3022	C–H stretching in ring [56,62]
3053	3040	3040	C–H stretching in ring [51,56,62]
	3109	3109	C–H stretching in ring [56,62]
	3130	3130	C–H stretching in ring [56,62]
3308			N–H stretching and bending vibration [51,56,62,64]

3.2. SEM/EDS

As shown in Figure 2, the elemental distribution of carbon in the TiN/C composite is uniform throughout the sample, while the distribution of Ti, N, and O were all associated with each other. The Ti, N, and O elements are dispersed homogenously throughout the sample except for the brighter areas where higher concentrations of Ti, N, and O are observed. The correlation of the Ti, N, and O maps indicates that the sample may consist of a

Ti–N–O, which was already observed in the literature [16,17]. Figure 3 shows the elemental distribution of C, V, N, and O in the VN/C composite, where carbon is distributed all over the sample. V, N, and O elements consistently appear to be co-located at specific sites across the mappings, which suggests that they are within the same compound [16,17].

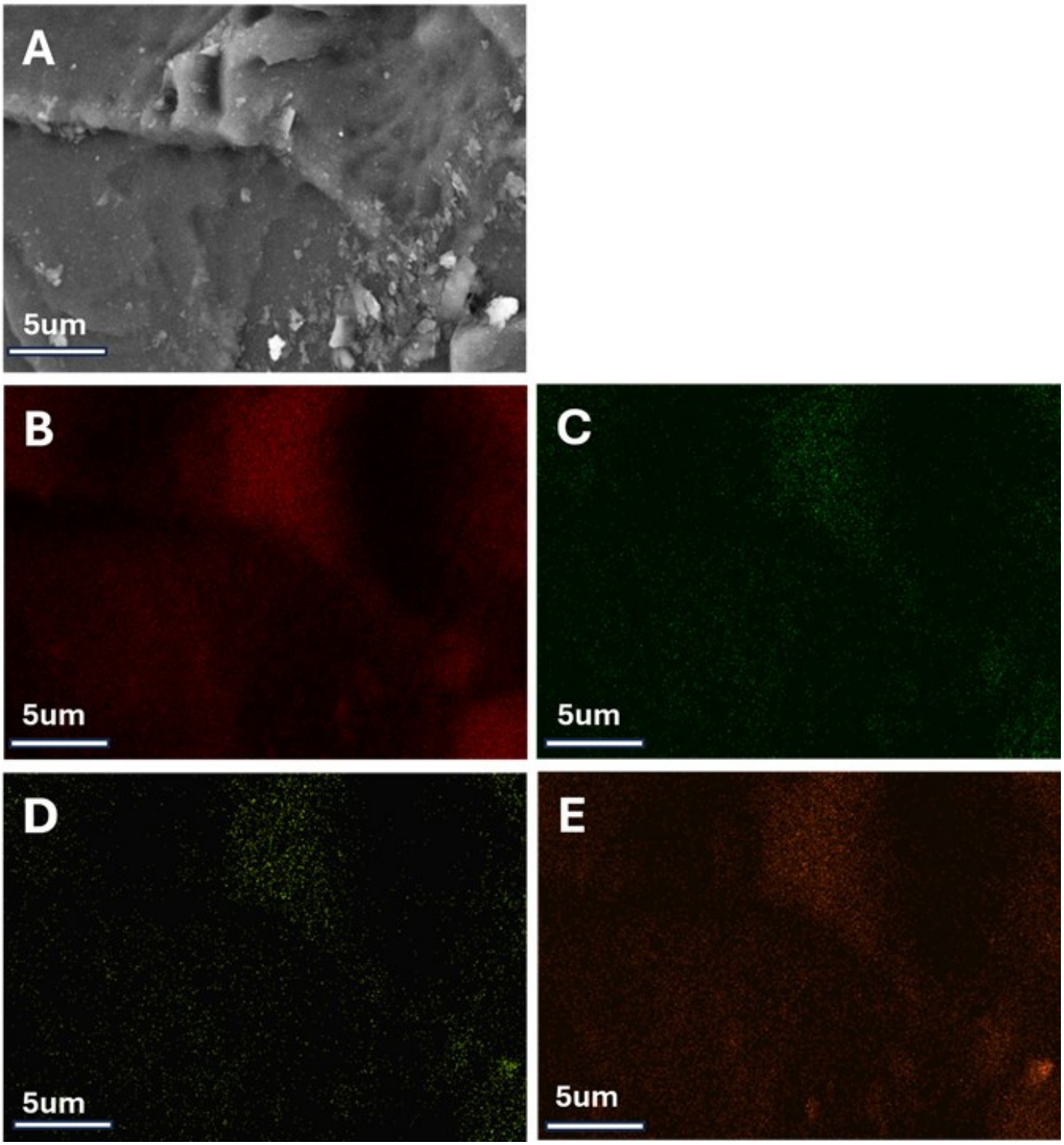

Figure 2. EDS mapping of the TiN/C composite sample showing the backscattered image (**A**), carbon (**B**), nitrogen (**C**), titanium (**D**), and oxygen (**E**).

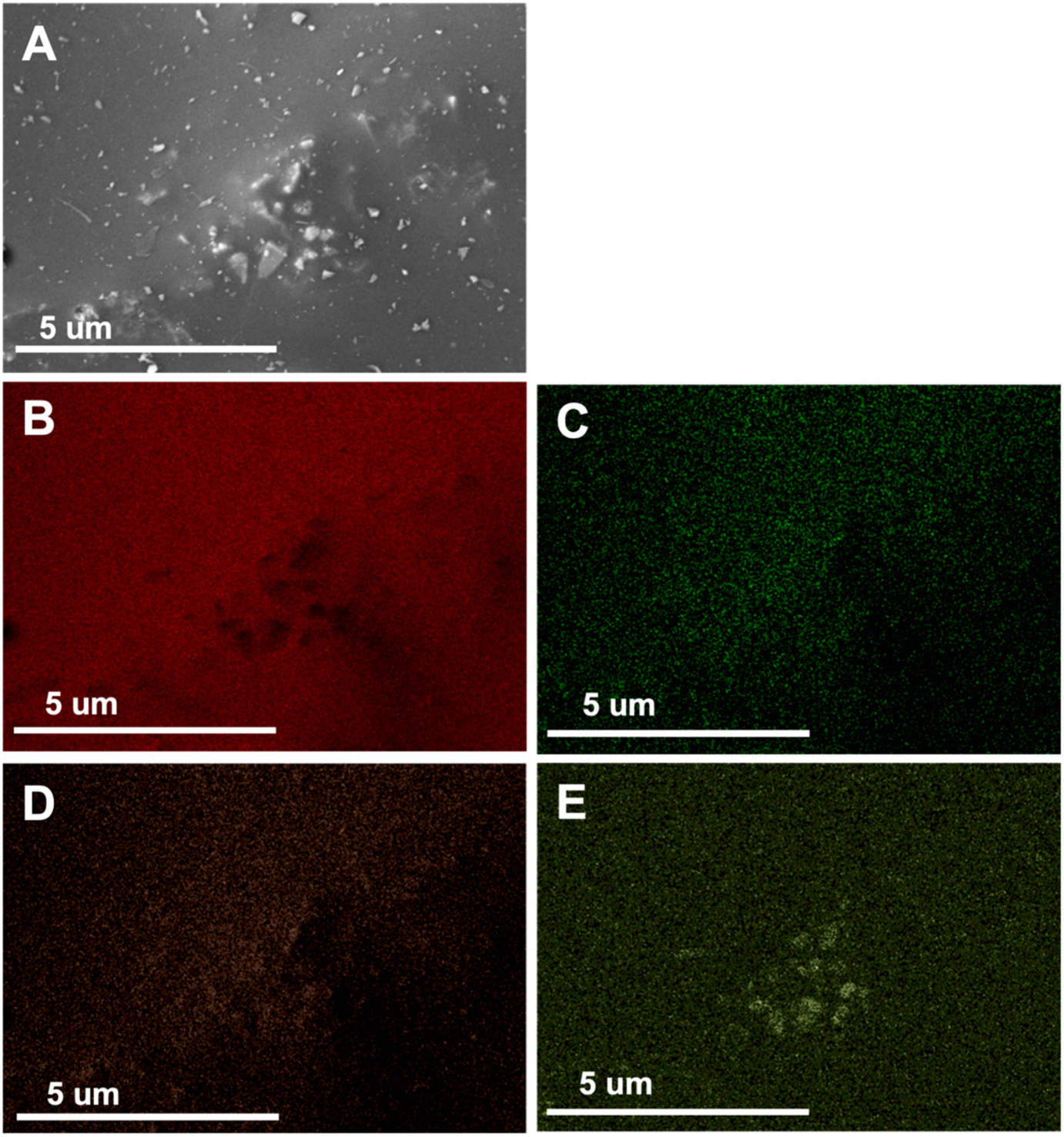

Figure 3. EDS mappings of the VN/C composite sample showing the backscattered image (**A**), carbon (**B**), nitrogen (**C**), vanadium (**D**), and oxygen (**E**).

3.3. TEM

The TEM images of the synthesized TiN/C composites are shown in Figure 4. The HRTEM of the synthesized TiN/C sample (Figure 4A) shows that the TiN nanoparticles appear to be clustered and supported within the carbon matrix. Figure 4B highlights one of the clusters, revealing that the larger particles are a collection of smaller crystalline nanoparticles with 5–10 nm in size. Figure 5 presents the HRTEM images of the VN/C showing VN nanoparticles throughout the sample (Figure 5A). In addition, the larger nanoparticles

appear to cluster together, displaying morphology similar to TiN/C. Figure 5B shows a higher magnification image of one of the clusters of crystalline nanoparticles with sizes ranging 5–10 nm.

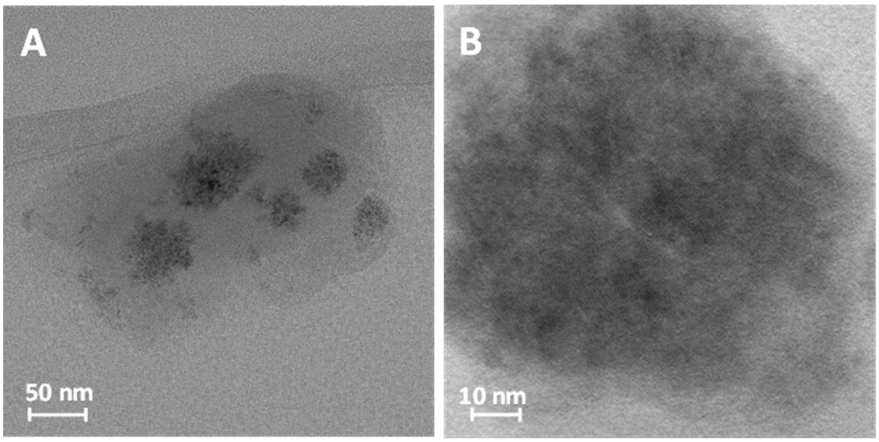

Figure 4. HRTEM images of TiN/C and VN/C samples at (**A**) 50 nm and (**B**) 10 nm.

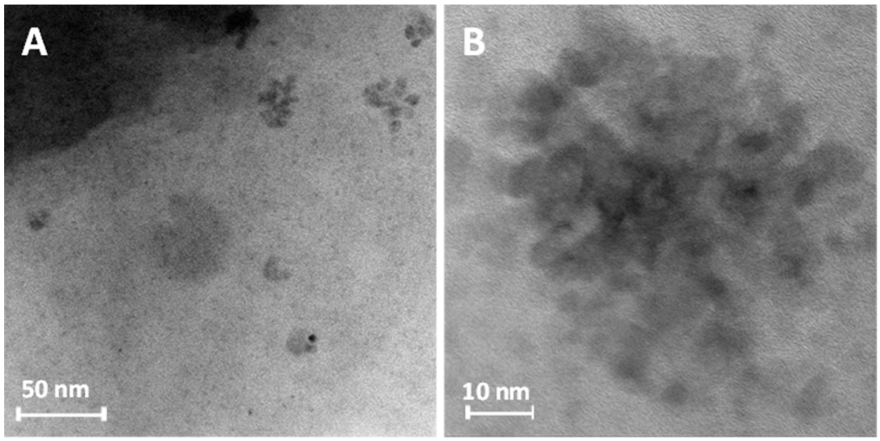

Figure 5. HRTEM images of VN/C sample at (**A**) 50 nm and (**B**) 10 nm.

3.4. XRD

The XRD patterns and Le Bail fitting for the H_2TPP, TiOTPP, and VOTTP samples are shown in Figure 6A–C, respectively. The associated fitting results and the determined lattice parameters are summarized in Table 2. The H_2TPP fitting results required two phases: the tetragonal ($I\bar{4}$) and the triclinic ($P\bar{1}$) for the H_2TPP crystals. The single-phase fitting had a χ^2 of 13.2; however, the addition of the second phase reduced the χ^2 to 2.90, indicating a good agreement between the fitting and the experimental data [41,42]. The $I\bar{4}$ phase was the major phase at approximately 90–95%. The lattice parameters are within the range of error for the Le Bail fitting procedure. The differences between the fitting and existing data in the literature appear in the second decimal point. The Le Bail fitting of the TiOTPP was found to be in the tetragonal phase with a space group of $I\bar{4}$ (a = b = 13.37, c = 9.94, and all angles were 90°). The C-axis was determined to be a little longer than that observed in the literature: 9.94 vs. 9.78 Å. However, the χ^2 of the TiOTPP fitting was 3.2, which was slightly larger than the other fittings but still indicated a good agreement between the data and the fitting. The VOTPP fitting was similar to that of TiOTPP with an $I\bar{4}$ lattice and lattice parameters a = b = 13.38 Å, a c = 9.76, and a χ^2 of 2.81. Figure 7 shows the powder XRD patterns for the TiN/C (A) and VN/C (B). The determined parameters for the Le Bail fittings are shown in Table 2. Both the thermally decomposed samples were found to fit well to the respective nitride lattices for TiN and VN. The TiN/C was determined to be in the $FM\bar{3}M$ crystal lattice with a = b = c = 4.24 Å with all the angles

equal to 90° and an χ^2 = 1.16 [17,44]. The XRD pattern of the VN/C nanocomposite sample was fitted using the VN lattice, which also has the $FM\bar{3}M$ lattice and a = b = c = 4.13 Å and all the angles = 90° and a χ^2 of 1.20 [16,45]. Both the XRD patterns of the TiN/C and VN/C samples have a large, broad peak around 29–31 in 2θ, which can be attributed to the disordered C 001 plane observed in amorphous carbon samples [16,17]. All fittings showed good agreement with the data reported in the literature, as was indicated by all the χ^2 values being below 5, which indicates that all the fittings are good and have low residuals [66,67].

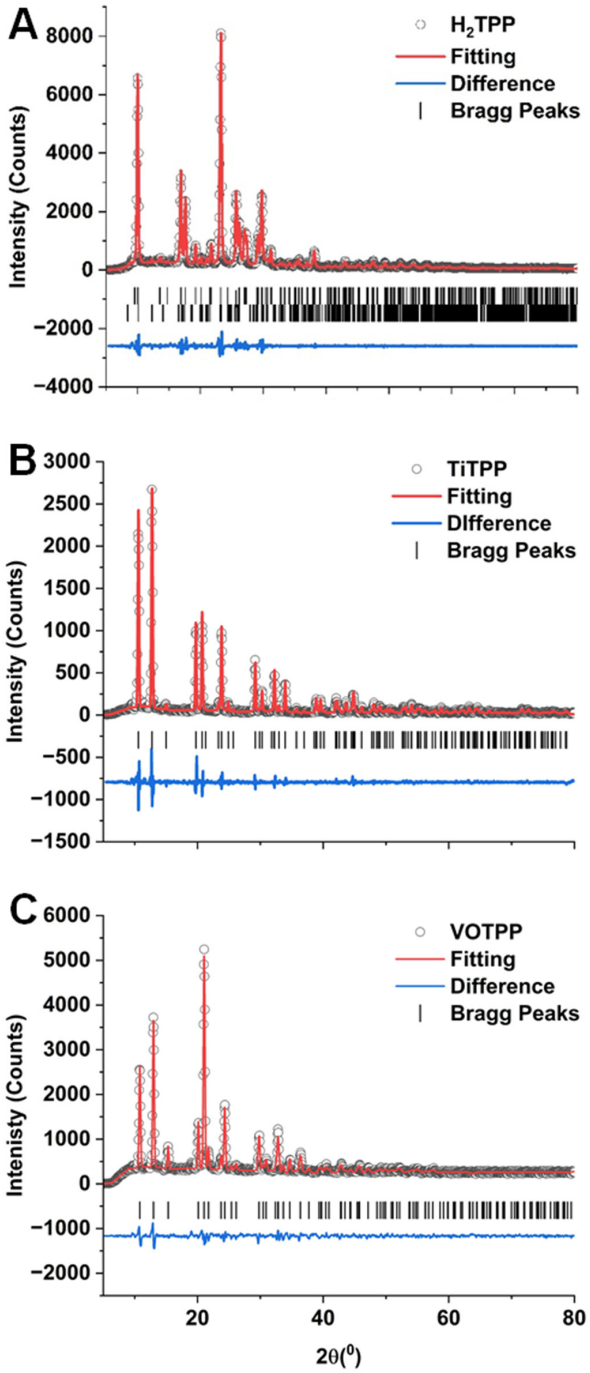

Figure 6. X-Ray diffraction patterns and Le Bail fitting of the H_2TPP (**A**), TiOTPP (**B**), and VOTPP (**C**).

Table 2. Le Bail fitting of the X-Ray diffraction patterns collected for H_2TPP, TiOTPP, VOTPP, TiN/C, and VN/C.

Compound	Space Group	a (Å)	b (Å)	c (Å)	α (°)	β (°)	γ (°)	χ^2	Reference
H_2TPP_{syn}	$I\bar{4}$	15.15	15.15	13.93	90.0	90.0	90.0	2.93	This work
H_2TPP_{syn}	$P\bar{1}$	6.44	10.44	12.39	95.9	99.0	101.26		This work
H_2TPP_{lit}	$I\bar{4}$	15.13	15.13	13.94	90.0	90.0	90.0	N/A	[41]
H_2TPP_{lit}	$P\bar{1}$	10.464	12.395	6.433	99.3	101.2	95.7	N/A	[42]
$TiOTPP_{syn}$	$I\bar{4}$	13.37	13.37	9.95	90.0	90.0	90.0		This work
$TiOTPP_{lit}$	$I\bar{4}$	13.379	13.379	9.776	90.0	90.0	90.0	N/A	[43]
TiN/C	$FM\bar{3}M$	4.24	4.24	4.24	90.0	90.0	90.0	1.16	This work
$TiN–C_{lit}$	$FM\bar{3}M$	4.24 (0)	4.24 (0)	4.24 (0)	90.0	90.0	90.0	1.50	[17]
TiN_{lit}	$FM\bar{3}M$	4.244	4.244	4.244	90.0	90.0	90.0	N/A	[44]
$VOTPP_{syn}$	$I\bar{4}$	13.34	13.34	9.75	90.0	90.0	90.0	2.81	This work
$VOTPP_{lit}$	$I\bar{4}$	13.34	13.34	9.75	90.0	90.0	90.0	N/A	[46]
VN/C	$FM\bar{3}M$	4.13	4.13	4.13	90.0	90.0	90.0	1.20	This work
$VN–C_{lit}$	$FM\bar{3}M$	4.13	4.13	4.13	90.0	90.0	90.0	N/A	[16]
VN_{lit}	$FM\bar{3}M$	4.13	4.13	4.13	90.0	90.0	90.0	N/A	[45]

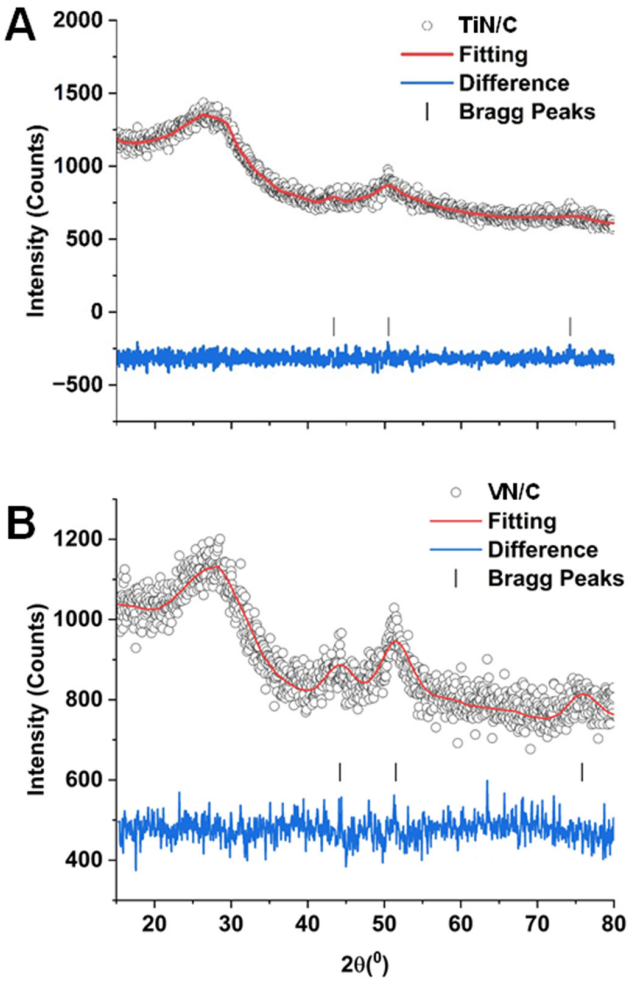

Figure 7. X-Ray diffraction patterns and Le Bail fitting of the TiN/C (**A**) and VN/C (**B**) samples.

3.5. XPS

Figures 8–11 present the high-resolution XPS spectra for TiOTPP, TiN/C, VOTPP, and VN/C, respectively. Table 3 shows the composition of the samples based on the atomic percentages from the XPS spectra analysis. The XPS data and bonding interactions associated with each peak are summarized in Tables 4 and 5 for the titanium and vanadium compounds, respectively.

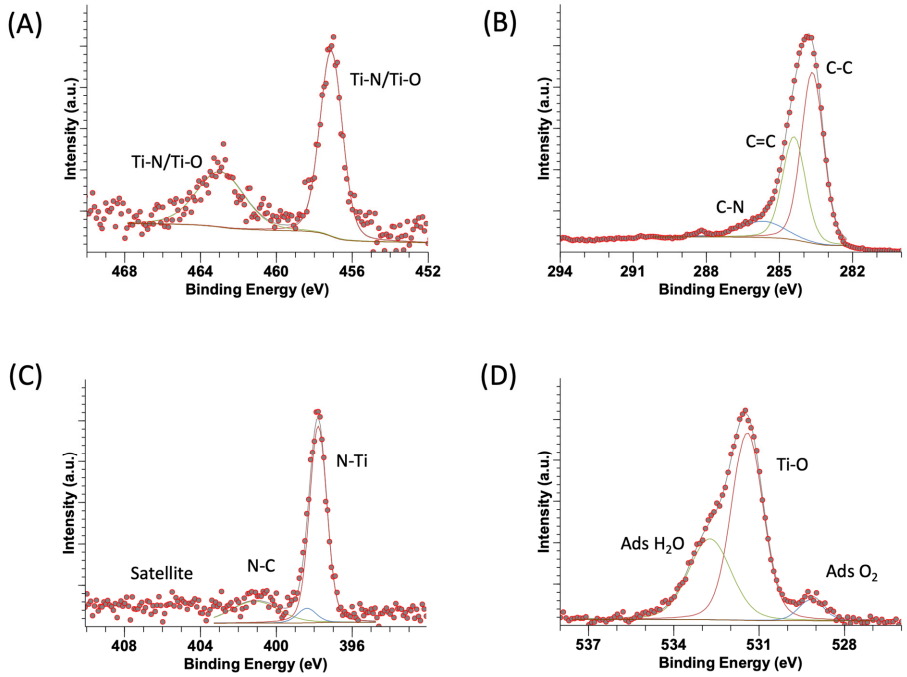

Figure 8. XPS spectra for TiOTPP (**A**) Ti 2p, (**B**) C 1s, (**C**) N 1s, (**D**) O 1s.

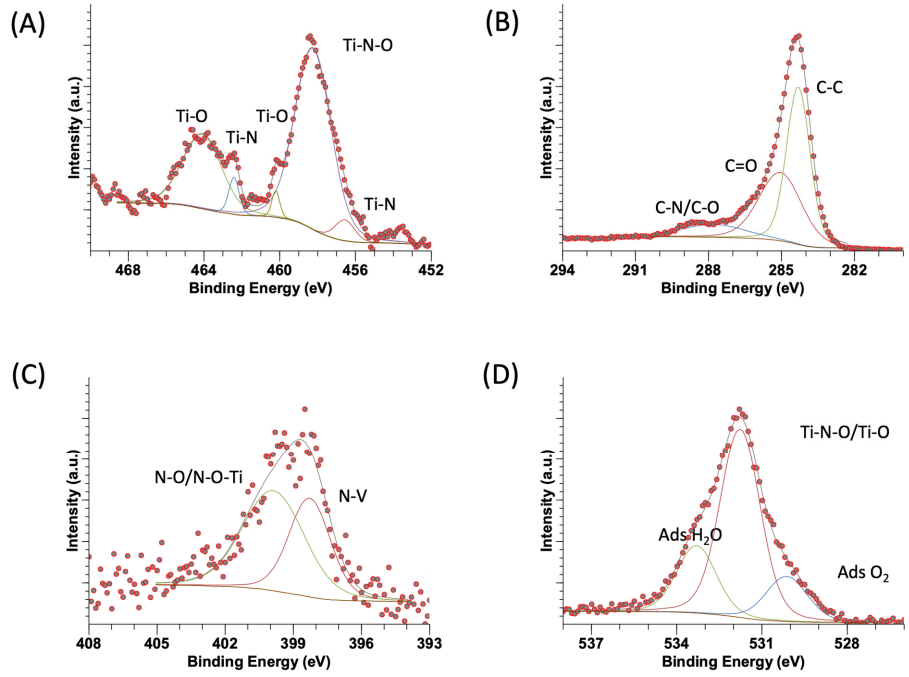

Figure 9. XPS spectra for TiN/C (**A**) Ti 2p, (**B**) C 1s, (**C**) N 1s, (**D**) O 1s.

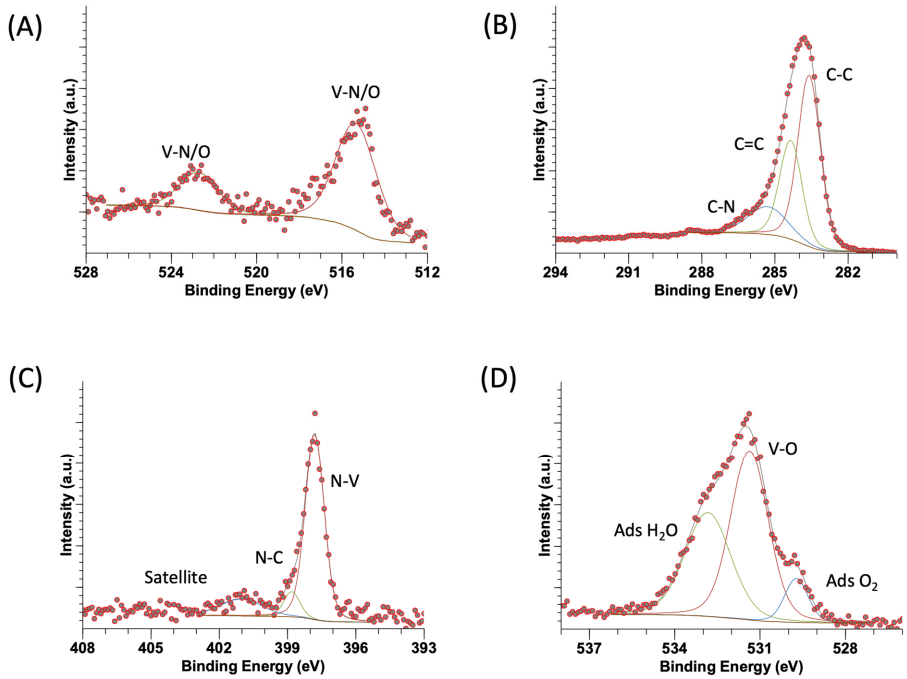

Figure 10. XPS spectra for VOTPP (**A**) V 2p, (**B**) C 1s, (**C**) N 1s, (**D**) O 1s.

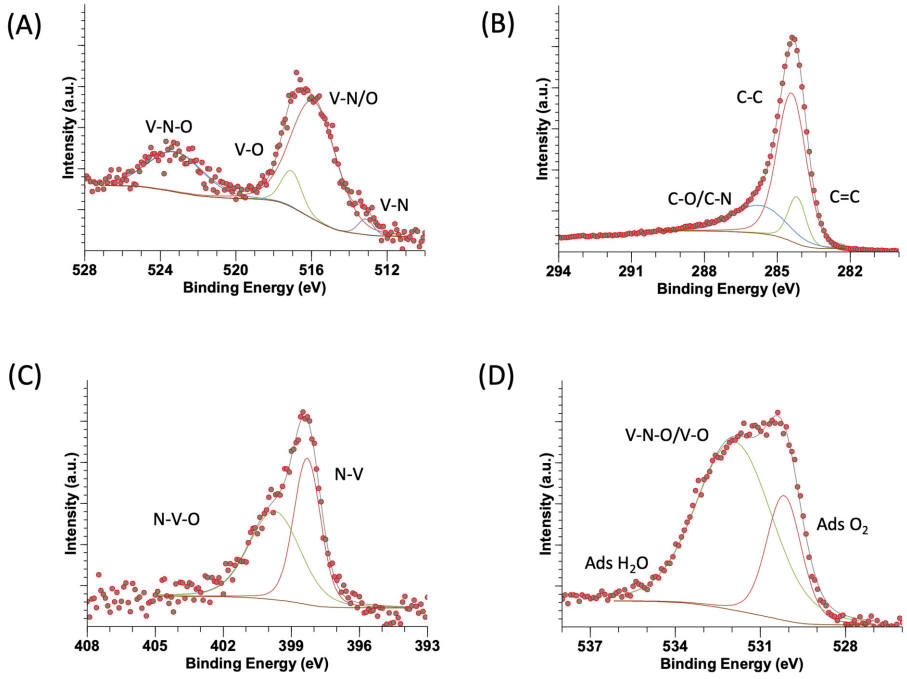

Figure 11. XPS spectra for VN/C (**A**) V 2p, (**B**) C 1s, (**C**) N 1s, (**D**) O 1s.

Table 3. Atomic composition based on the XPS analysis of the synthesized TiOTPP, VOTPP, TiN/C, and VN/C and TiN and VN synthesized using a sol–gel method [16,17].

Sample	% Ti	% N	% C	% O
TiOTPP	0.5	4.1	83.2	12.2
TiN/C	1.2	4.1	82.9	11.8
$TiN_{sol–gel}$	16.2	12.4	52.0	19.4
VOTPP	0.5	3.9	87.2	8.4
VN/C	0.7	2.6	91.8	4.9
$VN_{sol–gel}$	10.4	17.4	49.8	22.4

Table 4. Summary of the XPS fitting for the elements observed in TiOTPP, TiN/C, and $TiN(SG)_{lit}$ [17].

Sample	C 1s		O 1s		Ti $2p_{1/2}$		Ti $2p_{3/2}$		N 1s	
	Energy (eV)	State	Energy (eV)	State	Energy (eV)	State	Energy (eV)	State	Energy (eV)	State
TiOTPP	283.7	C–C	529.2	Ads O_2	457.1	Ti–N/O	463.0	Ti–N/O	397.8	N–Ti
	284.4	C=C	531.4	Ti–O					398.4	N–C
	285.7	C–N	532.7	Ads H_2O					401.1	Sat.
TiN/C	284.3	C=C	530.1	Ads O_2	456.6	Ti–N	460.2	Ti–O	398.3	N–Ti
	285.1	C–C	531.8	Ti–N–O/Ti–O	458.2	Ti–N–O	462.4	Ti–N	399.9	N–Ti–O
	287.8	C–O/C–N	533.3	Ads H_2O			464.1	Ti–O		
$TiN(SG)_{lit}$	284.8	C–C	529.9	Ads O_2	455.5	Ti–N	461.3	Ti–N	396.1	N–O–Ti
	286.1	C–O/C–N	531.7	O–N–Ti	456.7	Ti–N–O	469.3	Ti–O	397.1	N–Ti
	288.4	sat			458.4	Ti–O			398.8	N–O
									400.8	N=O

Table 5. Summary of the XPS fitting for the elements observed in VOTPP, VN/C, and $VN(SG)_{lit}$ [16].

Sample	C 1s		O 1s		V $2p_{1/2}$		V $2p_{3/2}$		N 1s	
	Energy (eV)	State	Energy (eV)	State	Energy (eV)	State	Energy (eV)	State	Energy (eV)	State
VOTPP	283.6	C–C	529.7	Ads O_2	515.3	V–N/O	522.7	V–N/O	397.8	N–V
	284.4	C=C	531.4	V–O					398.8	N–C
	285.3	C–N	532.8	Ads H_2O					401.0	Sat.
VN/C	284.4	C=C	530.1	Ads O_2	513.1	V–N	523.2	V–N–O	398.3	N–V
	285.2	C–C	531.8	V–N–O/V–O	515.9	V–N/O			399.3	V–N–O
	287.0	C–O/C–N	533.2	Ads H_2O	517.1	V–O				
$VN(SG)_{lit}$	284.2	C–C	529.8	Ads O_2	513.6	V–N	521.1	V–N	396.8	N–V
	285.4	C=C	531.2	O–N–V	515.3	V–N–O	523.7	V–N–O	399.0	V–N–O
	288.1	C–N/C–O			516.7	V–O			401.2	Sat.

Figure 8A shows the Ti 2p XPS spectrum for the TiOTPP precursor with two peaks at 457.1 and 463.0 eV, which corresponds to the Ti $2p_{1/2}$ and $2p_{3/2}$ regions, respectively, indicating the presence of the Ti^{4+} environment [68]. Figure 9A shows the Ti 2p XPS spectrum for the TiN/C composite. The $2p_{1/2}$ region was deconvolved into two peaks: 456.6 and 458.2 eV, identified as Ti^{3+}–N and Ti^{3+}–N–O environments, respectively. The $2p_{3/2}$ region was deconvolved in three peaks: 460.2, 462.4, and 464.1 eV, indicating the presence of Ti–O, Ti–N, and Ti–O environments, respectively [17,69–73]. Figure 8B shows the C 1s spectrum for TiOTPP where the region was deconvolved into three peaks at the following binding energies: 283.7, 284.4, and 285.7 eV, corresponding to the C–C, C=C, and C–N bonds, respectively [17,71,72,74]. Figure 9B shows the C 1s spectrum for the TiN/C composite. The XPS signal was deconvolved into three peaks: 284.3, 285.1, and 287.8 eV, which correspond to C=C, C–C, and C–O/C–N bonds, respectively [17,71,72,75,76]. Figure 8C shows the N 1s XPS spectrum for TiOTPP. The region was deconvolved into three peaks. A peak is present at 397.8 eV, indicating an N–Ti binding environment, at 398.4 eV, indicating an N–C binding environment, and a satellite peak located at 401.1 eV [72,77]. Figure 9C shows the N 1s region for the TiN/C sample, which was deconvolved into two peaks located at 398.3 and 399.9 eV. The peaks corresponded to N–Ti and N–O/N–O–Ti binding environments, respectively [17,73,78,79]. Figure 8D presents the O 1s XPS spectrum for the TiOTPP, which was deconvolved into three peaks: 529.2, 531.4, and 532.7 eV assigned to oxygen adsorbed on the surface, Ti–O, and water adsorbed, respectively [70,71,80–82]. Figure 9D shows the O 1s spectrum for the TiOTPP. The region was deconvolved into three peaks, 530.1, 531.8, and 533.3 eV, which were determined to be adsorbed oxygen on the surface, Ti–N–O/Ti–O and adsorbed water, respectively [69,70,79,80,82].

Figure 10A displays the vanadium spectra for the VOTPP precursor, which presents two peaks representing V $2p_{3/2}$ and V $2p_{1/2}$. The V $2p_{3/2}$ V $2p_{1/2}$ peaks were located at 515.3 and 522.7 eV, respectively [16,83]. Figure 11A shows the V 2p XPS spectrum for the VN/C composite. The V $2p_{1/2}$ region was deconvolved into three peaks, 513.1, 515.9, and 517.1 eV, which can be assigned to V–N, V–N/O, and V–O environments, respectively. The V $2p_{3/2}$ region was located at 523.2 eV [16,83]. Figure 10B shows the C 1s spectrum for VOTPP. The region was deconvolved into three peaks at binding energies: 283.6, 284.4, and 285.3 eV, corresponding to the C–C, C=C and C–N bonds, respectively [16,71,72,74]. Figure 11B shows the C 1s spectrum for the VN/C composite. The signal was deconvolved into three peaks: 284.4, 285.2, and 287.0 eV, corresponding to C=C, C–C, and C–O/C–N bonds, respectively [16,71,72,75]. Figure 10C shows the N 1s XPS spectrum for VOTPP. The region was deconvolved into three peaks. The peaks located at 397.8 and 398.8 correspond to an N–V and N–C environment, respectively. A satellite peak was located at 401.0 [72,84]. Figure 11C shows the N 1s region for the VN/C sample, which was deconvolved into two peaks located at 398.3 and 399.3 eV. The peaks corresponded to N–V and N–V–O binding environments, respectively [85,86]. Figure 10D presents the O 1s XPS spectrum for the VOTPP, which was deconvolved into three peaks: 529.7, 531.4, and 532.8 eV. The peaks were assigned to oxygen adsorbed on the surface, V–O, and adsorbed water, respectively [79,80,82,87]. Figure 11D shows the O 1s spectrum for the VN/C; the region was deconvolved into three peaks, 530.1, 531.8, and 533.2 eV, which were determined to be adsorbed oxygen on the surface, V–N–O/V–O and adsorbed water, respectively [79,80,83,86]. Due to the small particle sizes of the metal nitrides suspended in the carbon matrix, the surface of the nanoparticles is susceptible to surface oxidation under certain conditions, which may distort the XPS data interpretation. Potential oxidation during this analysis does not necessarily reflect the stability of the material; additional studies should be conducted to evaluate the stability of the material over time and under various environmental conditions.

4. Conclusions

Titanyl and Vanadyl tetraphenyl porphyrin are stable and well-known precursors for the synthesis of titanium and vanadium nitride carbon-based composites (TiN/C and

VN/C). The synthesis of TiOTPP and VOTPP was achieved using a slight modification to the methods in the literature, and their formation was confirmed using FTIR and XRD. The TiN and VN nanoparticles, entrapped in a carbon matrix, were prepared by the thermal decomposition of TiOTPP and VOTPP at 750 °C. TEM and SEM analyses revealed that the samples consisted of clusters and dispersed nanoparticles embedded within the carbon matrix. The decomposition process yielded the respective metal nitride (1:1 stoichiometry) in cubic form (space group of FM–3M). The XPS results confirmed the presence of the TiN and VN phases in the composite materials. This synthesis process is simple and rapid and results in a material with a relatively uniform distribution of the transition metal nitride within the carbon matrix. However, these are less uniformly distributed metal nitride particles in the carbon matrix, when compared to similarly synthesized metal nitride particles using phthalocyanine precursors [16,17]

Author Contributions: Conceptualization, H.M.M., M.A., and J.G.P.; Methodology, H.M.M., M.A., and J.G.P.; Formal Analysis, H.M.M., M.A., E.M.F., D.A.S., V.P.-G., M.O., and J.G.P.; Investigation, H.M.M., D.A.S., E.M.F., M.O., V.P.-G.; Resources, H.M.M., M.A., and J.G.P.; Data Curation, M.A., and J.G.P.; Writing—Original Draft Preparation, H.M.M.; Writing—Review & Editing, H.M.M., V.P.-G., M.O., M.A., and J.G.P.; Visualization, H.M.M.; Supervision, M.A., and J.G.P.; Project Administration, J.G.P.; Funding Acquisition, M.A., H.M.M., and J.G.P. All authors have read and agreed to the published version of the manuscript.

Funding: This research was funded by the Welch Foundation (BX-0048), the National Science Foundation grant (DMR-2122178 and DMR-2011401).

Data Availability Statement: All the relevant data that support the findings of this study are available from the corresponding authors on reasonable request.

Acknowledgments: J.G. Parsons and H.M. Morales are grateful and acknowledge the support provided by the Welch Foundation Grant (Grant No. BX-0048). M. Alcoutlabi acknowledges funding from the Partnership for Fostering Innovation by Bridging Excellence in Research and Student Success (NSF PREM, DMR-2122178). Part of this work was conducted at the College of Science and Engineering Characterization Facility, University of Minnesota, which received capital equipment funding from the NSF through the UMN MRSEC program (DMR-2011401).

Conflicts of Interest: The authors declare no conflict of interest.

References

1. IIdrees, M.; Mukhtar, A.; Ata-ur-Rehman; Abbas, S.M.; Zhang, Q.; Li, X. Transition metal nitride electrodes as future energy storage devices: A review. *Mater. Today Commun.* **2021**, *27*, 102363. [CrossRef]
2. Gao, B.; Li, X.; Ding, K.; Huang, C.; Li, Q.; Chu, P.K.; Huo, K. Recent progress in nanostructured transition metal nitrides for advanced electrochemical energy storage. *J. Mater. Chem. A* **2019**, *7*, 14–37. [CrossRef]
3. Balogun, M.-S.; Qiu, W.; Wang, W.; Fang, P.; Lu, X.; Tong, Y. Recent advances in metal nitrides as high-performance electrode materials for energy storage devices. *J. Mater. Chem. A* **2015**, *3*, 1364–1387. [CrossRef]
4. Hao, W.; Li, J.; Li, K.; Lin, Y.; Chen, J.; Gao, L.; Nicolosi, V.; Xiao, X.; Lee, J.-M. Transition metal nitrides for electrochemical energy applications. *Chem. Soc. Rev.* **2021**, *50*, 1354–1390.
5. Nzereogu, P.U.; Omah, A.D.; Ezema, F.I.; Iwuoha, E.I.; Nwanya, A.C. Anode materials for lithium-ion batteries: A review. *Appl. Surf. Sci. Adv.* **2022**, *9*, 100233. [CrossRef]
6. Dhar, S.P.D.; Murthy, Z.V.P.; Kailasa, S.K. Metal nitrides nanostructures: Properties, synthesis and conceptualization in analytical methods developments for chemical analysis and separation, and in energy storage applications. *Coord. Chem. Rev.* **2023**, *481*, 215046.
7. Yu, Z.; Xia, X.; Shi, F.; Zhan, J.; Tu, J.; Fan, H.J. Transition Metal Carbides and Nitrides in Energy Storage and Conversion. *Adv. Sci.* **2016**, *3*, 1500286.
8. Cheng, Z.; Qi, W.; Pang, C.H.; Thomas, T.; Wu, T.; Liu, S.; Yang, M. Recent Advances in Transition Metal Nitride-Based Materials for Photocatalytic Applications. *Adv. Funct. Mater.* **2021**, *31*, 2100553. [CrossRef]
9. Yue, Y.; Han, P.; He, X.; Zhang, K.; Liu, Z.; Zhang, C.; Dong, S.; Gu, L.; Cui, G. In situ synthesis of a graphene/titanium nitride hybrid material with highly improved performance for lithium storage. *J. Mater. Chem.* **2012**, *22*, 4938–4943. [CrossRef]
10. Ashraf, I.; Rizwan, S.; Iqbal, M. A Comprehensive Review on the Synthesis and Energy Applications of Nano-structured Metal Nitrides. *Front. Mater.* **2020**, *7*, 181. [CrossRef]
11. Balogun, M.-S.; Huang, Y.; Qiu, W.; Yang, H.; Ji, H.; Tong, Y. Updates on the development of nanostructured transition metal nitrides for electrochemical energy storage and water splitting. *Mater. Today* **2017**, *20*, 425–451. [CrossRef]

12. Dong, Y.; Li, Y.; Shi, H.; Qin, J.; Zheng, S.; He, R.; Wu, Z.-S. Graphene encapsulated iron nitrides confined in 3D carbon nanosheet frameworks for high-rate lithium ion batteries. *Carbon* **2020**, *159*, 213–220. [CrossRef]
13. Pan, X.; Song, X.; Lin, S.; Bi, K.; Hao, Y.; Du, Y.; Liu, J.; Fan, D.; Wang, Y.; Lei, M. A facile route to graphite-tungsten nitride and graphite-molybdenum nitride nanocomposites and their ORR performances. *Ceram. Int.* **2016**, *42*, 16017–16022. [CrossRef]
14. Ji, L.; Lin, Z.; Alcoutlabi, M.; Zhang, X. Recent developments in nanostructured anode materials for rechargeable lithium-ion batteries. *Energy Environ. Sci.* **2011**, *4*, 2682–2699. [CrossRef]
15. Flores, D.; Villarreal, J.; Lopez, J.; Alcoutlabi, M. Production of carbon fibers through Forcespinning® for use as anode materials in sodium ion batteries. *Mater. Sci. Eng. B* **2018**, *236–237*, 70–75. [CrossRef]
16. Morales, H.M.; Vieyra, H.; Sanchez, D.A.; Fletes, E.M.; Odlyzko, M.; Lodge, T.P.; Padilla-Gainza, V.; Alcoutlabi, M.; Parsons, J.G. Synthesis and Characterization of Vanadium Nitride/Carbon Nanocomposites. *Int. J. Mol. Sci.* **2024**, *25*, 6952. [CrossRef]
17. Morales, H.M.; Vieyra, H.; Sanchez, D.A.; Fletes, E.M.; Odlyzko, M.; Lodge, T.P.; Padilla-Gainza, V.; Alcoutlabi, M.; Parsons, J.G. Synthesis and Characterization of Titanium Nitride–Carbon Composites and Their Use in Lithium-Ion Batteries. *Nanomaterials* **2024**, *14*, 624. [CrossRef]
18. Luo, Q.; Lu, C.; Liu, L.; Zhu, M. A review on the synthesis of transition metal nitride nanostructures and their energy related applications. *Green. Energy Environ.* **2023**, *8*, 406–437. [CrossRef]
19. Wen, Z.; Cui, S.; Pu, H.; Mao, S.; Yu, K.; Feng, X.; Chen, J. Metal Nitride/Graphene Nanohybrids: General Synthesis and Multifunctional Titanium Nitride/Graphene Electrocatalyst. *Adv. Mater.* **2011**, *23*, 5445–5450. [CrossRef]
20. Jun, Y.-S.; Hong, W.H.; Antonietti, M.; Thomas, A. Mesoporous, 2D Hexagonal Carbon Nitride and Titanium Nitride/Carbon Composites. *Adv. Mater.* **2009**, *21*, 4270–4274. [CrossRef]
21. Cheng, H.; Garcia-Araez, N.; Hector, A.L. Synthesis of Vanadium Nitride–Hard Carbon Composites from Cellulose and Their Performance for Sodium-Ion Batteries. *ACS Appl. Energy Mater.* **2020**, *3*, 4286–4294. [CrossRef]
22. Yang, Y.; Zhao, L.; Shen, K.; Liu, Y.; Zhao, X.; Wu, Y.; Wang, Y.; Ran, F. Ultra-small vanadium nitride quantum dots embedded in porous carbon as high performance electrode materials for capacitive energy storage. *J. Power Sources* **2016**, *333*, 61–71. [CrossRef]
23. Yang, Y.; Shen, K.; Liu, Y.; Tan, Y.; Zhao, X.; Wu, J.; Niu, X.; Ran, F. Novel Hybrid Nanoparticles of Vanadium Nitride/Porous Carbon as an Anode Material for Symmetrical Supercapacitor. *Nano-Micro. Lett.* **2016**, *9*, 6. [CrossRef]
24. Yousefi, E.; Ghorbani, M.; Dolati, A.; Yashiro, H. Facile synthesis of titanium nitride-graphene nanocomposite and its improved rate-dependent electroactivity with respect to lithium storage. *Mater. Res. Bull.* **2016**, *84*, 388–396. [CrossRef]
25. Shiva, S.G.; Markad, G.B.; Jagadeeswararao, M.; Bansode, U.; Nag, A. Colloidal Nanocomposite of TiN and N-Doped Few-Layer Graphene for Plasmonics and Electrocatalysis. *ACS Energy Lett.* **2017**, *2*, 2251–2256.
26. Sun, Z.; Zhang, J.; Yin, L.; Hu, G.; Fang, R.; Cheng, H.-M.; Li, F. Conductive porous vanadium nitride/graphene composite as chemical anchor of polysulfides for lithium-sulfur batteries. *Nat. Commun.* **2017**, *8*, 14627. [CrossRef]
27. Li, C.; Zhu, L.; Qi, S.; Ge, W.; Ma, W.; Zhao, Y.; Huang, R.; Xu, L.; Qian, Y. Ultrahigh-Areal-Capacity Battery Anodes Enabled by Free-Standing Vanadium Nitride@N-Doped Carbon/Graphene Architecture. *ACS Appl. Mater. Interfaces* **2020**, *12*, 49607–49616. [CrossRef]
28. Zhang, K.; Wang, H.; He, X.; Liu, Z.; Wang, L.; Gu, L.; Xu, H.; Han, P.; Dong, S.; Zhang, C.; et al. A hybrid material of vanadium nitride and nitrogen-doped graphene for lithium storage. *J. Mater. Chem.* **2011**, *21*, 11916–11922. [CrossRef]
29. Balamurugan, J.; Karthikeyan, G.; Thanh, T.D.; Kim, N.H.; Lee, J.H. Facile synthesis of vanadium nitride/nitrogen-doped graphene composite as stable high performance anode materials for supercapacitors. *J. Power Sources* **2016**, *308*, 149–157. [CrossRef]
30. Yuan, W.; Cheng, L.; Wu, H.; Zhang, Y.; Lv, S.; Guo, X. One-step synthesis of 2D-layered carbon wrapped transition metal nitrides from transition metal carbides (MXenes) for supercapacitors with ultrahigh cycling stability. *Chem. Commun.* **2018**, *54*, 2755–2758. [CrossRef] [PubMed]
31. Liu, Y.; Shen, Y.; Zhu, S.; Li, D. TiN nanoparticles hybridized with Fe, N co-doped carbon nanosheets composites as highly efficient electrocatalyst for oxygen reduction reaction. *Chem. Eng. J.* **2020**, *400*, 125968. [CrossRef]
32. Lia, Q.; Chena, Y.; Zhanga, J.; Tiana, W.; Wanga, L.; Rena, Z.; Rena, X.; Lib, X.; Gaob, B.; Pengc, X.; et al. Spatially confined synthesis of vanadium nitride nanodots intercalated carbon nanosheets with ultrahigh volumetric capacitance and long life for flexible supercapacitors. *Nano Energy* **2018**, *51*, 128–136. [CrossRef]
33. Ouldhamadouche, N.; Achour, A.; Lucio-Porto, R.; Islam, M.; Solaymani, S.; Arman, A.; Ahmadpourian, A.; Achour, H.; Le Brizoual, L.; Djouadi, M.A.; et al. Electrodes based on nano-tree-like vanadium nitride and carbon nanotubes for micro-supercapacitors. *J. Mater. Sci. Technol.* **2018**, *34*, 976–982. [CrossRef]
34. Huang, J.; Peng, Z.; Xiao, Y.; Xu, Y.; Chen, L.; Xiong, Y.; Tan, L.; Yuan, K.; Chen, Y. Hierarchical Nanosheets/Walls Structured Carbon-Coated Porous Vanadium Nitride Anodes Enable Wide-Voltage-Window Aqueous Asymmetric Supercapacitors with High Energy Density. *Adv. Sci.* **2019**, *6*, 982–988. [CrossRef] [PubMed]
35. Xiao, X.; Peng, X.; Jin, H.; Li, T.; Zhang, C.; Gao, B.; Hu, B.; Huo, K.; Zhou, J. Freestanding mesoporous VN/CNT hybrid electrodes for flexible all-solid-state supercapacitors. *Adv. Mater.* **2013**, *25*, 5091–5097. [CrossRef]
36. Ghimbeu, C.M.; Raymundo-Piñero, E.; Fioux, P.; Béguin, F.; Vix-Guterl, C. Vanadium nitride/carbon nanotube nanocomposites as electrodes for supercapacitors. *J. Mater. Chem.* **2011**, *21*, 13268–13275. [CrossRef]

37. Jia, H.; Cai, Y.; Li, S.; Zheng, X.; Miao, L.; Wang, Z.; Qi, J.; Cao, J.; Feng, J.; Fei, W. In situ synthesis of core-shell vanadium nitride@N-doped carbon microsheet sponges as high-performance anode materials for solid-state supercapacitors. *J. Colloid. Interface Sci.* **2020**, *560*, 122–129. [CrossRef]
38. Adler, A.D.; Longo, F.R.; Finarelli, J.D.; Goldmacher, J.; Assour, J.; Korsakoff, L. A simplified synthesis for meso-tetraphenylporphine. *J. Org. Chem.* **1967**, *32*, 476. [CrossRef]
39. Wong, S.-Y.; Sun, R.W.-Y.; Chung, N.P.-Y.; Lin, C.-L.; Che, C.-M. Physiologically stable vanadium(iv) porphyrins as a new class of anti-HIV agents. *Chem. Commun.* **2005**, 3544–3546. [CrossRef]
40. Rodríguez-Carvajal, J. Recent advances in magnetic structure determination by neutron powder diffraction. *Phys. B Condens. Matter* **1993**, *192*, 55–69. [CrossRef]
41. Hamor, M.J.; Hamor, T.A.; Hoard, J.L. The Structure of Crystalline Tetraphenylporphine. The Stereochemical Nature of the Porphine Skeleton. *J. Am. Chem. Soc.* **1964**, *86*, 1938–1942. [CrossRef]
42. Kano, K.; Fukuda, K.; Wakami, H.; Nishiyabu, R.; Pasternack, R.F. Factors Influencing Self-Aggregation Tendencies of Cationic Porphyrins in Aqueous Solution. *J. Am. Chem. Soc.* **2000**, *122*, 7494–7502. [CrossRef]
43. Yamabayashi, T.; Atzori, M.; Tesi, L.; Cosquer, G.; Santanni, F.; Boulon, M.-E.; Morra, E.; Benci, S.; Torre, R.; Chiesa, M.; et al. Scaling Up Electronic Spin Qubits into a Three-Dimensional Metal–Organic Framework. *J. Am. Chem. Soc.* **2018**, *140*, 12090–12101. [CrossRef] [PubMed]
44. Brager, A. An X-ray examination of titanium nitride. *Acta Physicochim. (USSR)* **1939**, *9*, 617–632.
45. Brauer, G.; Schnell, W.D. Zur kenntnis des Systems Vanadium-Stickstoff und des reinen vanadiums. *J. Less Common. Met.* **1964**, *6*, 326–332. [CrossRef]
46. Drew, M.G.B.; Mitchell, P.C.H.; Scott, C.E. Crystal and molecular structure of three oxovanadium(IV) porphyrins: Oxovanadium tetraphenylporphyrin(I), oxovanadium(IV) etioporphyrin(II) and the 1:2 adduct of (II) with 1,4-dihydroxybenzene(III). Hydrogen bonding involving the VO group. Relevance to ca. *Inorganica Chim. Acta* **1984**, *82*, 63–68. [CrossRef]
47. Fairley, N.; Fernandez, V.; Richard-Plouet, M.; Guillot-Deudon, C.; Walton, J.; Smith, E.; Flahaut, D.; Greiner, M.; Biesinger, M.; Tougaard, S.; et al. Systematic and collaborative approach to problem solving using X-ray photoelectron spectroscopy. *Appl. Surf. Sci. Adv.* **2021**, *5*, 100112. [CrossRef]
48. Saini, G.S.; Sharma, S.; Kaur, S.; Tripathi, S.K.; Mahajan, C.G. Infrared spectroscopic studies of free-base tetraphenylporphine and its dication. *Spectrochim. Acta Part A Mol. Biomol. Spectrosc.* **2005**, *61*, 3070–3076. [CrossRef]
49. Nadeem, S.; Mutalib, M.I.A.; Shaharum, M.S. One pot synthesis and characterization of meso-5, 10, 15, 20-copper tetraphenylporphyrin. *J. Chem.* **2016**, *9*, 309–314.
50. Neamtu, M.; Nadejde, C.; Brinza, L.; Dragos, O.; Gherghel, D.; Paul, A. Iron phthalocyanine-sensitized magnetic catalysts for BPA photodegradation. *Sci. Rep.* **2020**, *10*, 5376. [CrossRef]
51. Al Neyadi, S.S.; Alzamly, A.; Al-Hemyari, A.; Tahir, I.M.; Al-Meqbali, S.; Ahmad, M.A.A.; Bufaroosha, M. An Undergraduate Experiment Using Microwave-Assisted Synthesis of Metalloporphyrins: Characterization and Spectroscopic Investigations. *World J. Chem. Educ.* **2019**, *7*, 26–32. [CrossRef]
52. Harbeck, S.; Mack, H. *Experimental and Theoretical Investigations on the IR and Raman Spectra for CuPc and TiOPC*; Universitat Tubingen: Tübingen, Germany, 2013.
53. Goedken, V.L.; Dessy, G.; Ercolani, C.; Fares, V. Synthesis, reactivity, and x-ray crystal structure of dichloro(phthalocyaninato) titanium(IV). *Inorg. Chem.* **1985**, *24*, 991–995. [CrossRef]
54. Song, K.; Tang, C.; Zou, Z.; Wu, Y. Modification of porous lignin with metalloporphyrin as an efficient catalyst for the synthesis of cyclic carbonates. *Transit. Met. Chem.* **2020**, *45*, 111–119. [CrossRef]
55. Tonezzer, M.; Maggioni, G.; Dalcanale, E. Production of novel microporous porphyrin materials with superior sensing capabilities. *J. Mater. Chem.* **2012**, *22*, 5647–5655. [CrossRef]
56. Quiroz-Segoviano, R.I.Y.; García-Sánchez, M.A.; Delgado-Buenrostro, N.L.; Chirino, Y.I.; Bernal-Chávez, S.; Nava-Arzaluz, M.G.; Ganem-Rondero, A. Tetraphenylporphyrin intended for use in photodynamic therapy: Influence of sonophoresis and the formulation (solution or microemulsion) on percutaneous penetration. *J. Drug Deliv. Sci. Technol.* **2019**, *53*, 101145. [CrossRef]
57. Ross, A.; Soares, D.C.; Covelli, D.; Pannecouque, C.; Budd, L.; Collins, A.; Robertson, N.; Parsons, S.; De Clercq, E.; Kennepohl, P.; et al. Oxovanadium(IV) cyclam and bicyclam complexes: Potential CXCR4 receptor. *Inorg. Chem.* **2010**, *49*, 1122–1132. [CrossRef] [PubMed]
58. Chen, H.; Yang, Z.; We, R.; Tan, Z. Stabilization of potassium ferrate cathodic material coated with tetraphenylporphyrin. *Electrochim. Acta* **2012**, *75*, 62–70. [CrossRef]
59. Chen, W.; Suenobu, T.; Fukuzumi, S. A Vanadium Porphyrin with Temperature-Dependent Phase Transformation: Synthesis, Crystal Structures, Supramolecular Motifs and Properties. *Chem.—Asian J.* **2011**, *6*, 1416–1422. [CrossRef]
60. Abood, E.; Al-Ahmad, A.; Hussein, A.; Hassan, Q.; Sultan, A.; Almowali, A. Low Optical Limiting and Nonlinear Optical Properties of Vanadyl Phthalocyanine using a CW Laser. *Chem. Mater. Res.* **2013**, *3*, 18–25.
61. Ageeva, T.A.; Golubev, D.V.; Gorshkova, A.S.; Ionov, A.M.; Kopylova, E.V.; Koifman, O.I.; Mozhchil, R.N.; Rozhkova, E.P.; Rumyantseva, V.D.; Sigov, A.S.; et al. XPS and IR Spectroscopic Studies of Titanyl and Vanadyl Complexes. *Macroheterocycles* **2019**, *12*, 148–153. [CrossRef]
62. Pop, S.-F.; Ion, R.-M.; Corobea, M.C.; Raditoiu, V. Spectral and thermal investigations of porphyrin and phthalocyanine nanomaterials. *J. Optoelectron. Adv. Mater.* **2011**, *13*, 906–911.

63. Moghadam, M.; Mohammadpoor-Baltork, I.; Tangestaninejad, S.; Mirkhani, V.; Khosropour, A.R.; Taghavi, S.A. Electron-deficient vanadium(IV) tetraphenylporphyrin: A new, highly efficient and reusable catalyst for chemoselective trimethylsilylation of alcohols and phenols with hexamethyldisilazane. *Appl. Organomet. Chem.* **2011**, *25*, 687–694. [CrossRef]
64. Sun, Z.-C.; She, Y.-B.; Song, X.-F.; Li, K. Synthesis, characterization and spectral properties of substituted tetraphenylporphyrin iron chloride complexes. *Molecules* **2011**, *16*, 2960–2970. [CrossRef]
65. Kubendhiran, S.; Sakthinathan, S.; Chen, S.-M.; Tamizhdurai, P.; Shanthi, K.; Karuppiah, C. Green reduction of reduced graphene oxide with nickel tetraphenyl porphyrin nanocomposite modified electrode for enhanced electrochemical determination of environmentally pollutant nitrobenzene. *J. Colloid. Interface Sci.* **2017**, *497*, 207–216. [CrossRef] [PubMed]
66. Botez, C.E.; Morris, J.L.; Manriquez, A.J.E.; Anchondo, A. Heating induced structural and chemical behavior of KD2PO4 in the 25 °C–215 °C temperature range. *Mater. Charact.* **2013**, *83*, 74–78. [CrossRef]
67. Blowey, P.J.; Maurer, R.J.; Rochford, L.A.; Duncan, D.A.; Kang, J.H.; Warr, D.A.; Ramadan, A.J.; Lee, T.L.; Thakur, P.K.; Costantini, G.; et al. The Structure of VOPc on Cu(111): Does V═O Point Up, or Down, or Both? *J. Phys. Chem. C* **2019**, *123*, 8101–8111. [CrossRef]
68. Shi, P.; Song, Y.; Tang, J.; Nie, Z.; Chang, J.; Chen, Q.; He, Y.; Guo, T.; Zhang, J.; Wang, H. Ultra-narrow bandwidth red-emission carbon quantum dots and their bio-imaging. *Phys. E Low-Dimens. Syst. Nanostructures* **2022**, *142*, 115197. [CrossRef]
69. Shen, H.; Wang, L. Corrosion resistance and electrical conductivity of plasma nitrided titanium. *Int. J. Hydrogen Energy* **2021**, *46*, 11084–11091. [CrossRef]
70. Chan, M.-H.; Lu, F.-H. X-ray photoelectron spectroscopy analyses of titanium oxynitride films prepared by magnetron sputtering using air/Ar mixtures. *Thin Solid. Film.* **2009**, *517*, 5006–5009. [CrossRef]
71. Cheng, H.; Garcia-Araez, N.; Hector, A.L.; Soulé, S. Synthesis of Hard Carbon-TiN/TiC Composites by Reacting Cellulose with TiCl4 Followed by Carbothermal Nitridation/Reduction. *Inorg. Chem.* **2019**, *58*, 5776–5786. [CrossRef]
72. Mondol, M.M.H.; Kim, C.-U.; Jhung, S.H. Titanium nitride@nitrogen-enriched porous carbon derived from metal–organic frameworks and melamine: A remarkable oxidative catalyst to remove indoles from fuel. *Chem. Eng. J.* **2022**, *450*, 138411. [CrossRef]
73. Beaudette, C.A.; Tu, Q.; Eslamisaray, M.A.; Kortshagen, U.R. Plasma-Synthesized Nitrogen-Doped Titanium Dioxide Nanoparticles With Tunable Visible Light Absorption and Photocatalytic Activity. *ASME Open J. Eng.* **2022**, *1*, 2770–3495. [CrossRef]
74. Edmondson, M.; Frampton, E.S.; Judd, C.J.; Champness, N.R.; Jones, R.G.; Saywell, A. Order, disorder, and metalation of tetraphenylporphyrin (2H-TPP) on Au(111). *Chem. Commun.* **2022**, *58*, 6247–6250. [CrossRef] [PubMed]
75. Farahmand, S.; Ghiaci, M.; Asghari, S. Oxo-vanadium (IV) phthalocyanine implanted onto the modified SBA-15 as a catalyst for direct hydroxylation of benzene to phenol in acetonitrile-water medium: A kinetic study. *Chem. Eng. Sci.* **2021**, *232*, 116331. [CrossRef]
76. Fan, J.-M.; Chen, J.-J.; Zhang, Q.; Chen, B.-B.; Zang, J.; Zheng, M.-S.; Dong, Q.-F. An Amorphous Carbon Nitride Composite Derived from ZIF-8 as Anode Material for Sodium-Ion Batteries. *ChemSusChem* **2015**, *8*, 1856–1861. [CrossRef] [PubMed]
77. Shubina, T.E.; Marbach, H.; Flechtner, K.; Kretschmann, A.; Jux, N.; Buchner, F.; Steinruck, H.P.; Clark, T.; Gottfried, J.M. Principle and mechanism of direct porphyrin metalation: Joint experimental and theoretical investigation. *J. Am. Chem. Soc.* **2007**, *129*, 9476–9483. [CrossRef]
78. Jaeger, D.; Patscheider, J. A complete and self-consistent evaluation of XPS spectra of TiN. *J. Electron. Spectrosc. Relat. Phenom.* **2012**, *185*, 523–534. [CrossRef]
79. Mucha, N.R.; Som, J.; Shaji, S.; Fialkova, S.; Apte, P.R.; Balasubramanian, B.; Shield, J.E.; Anderson, M.; Kumar, D. Electrical and optical properties of titanium oxynitride thin films. *J. Mater. Sci.* **2020**, *55*, 5123–5134. [CrossRef]
80. Norton, P.R. An investigation of the adsorption of oxygen and oxygen containing species on platinum by photoelectron spectroscopy. *Surf. Sci.* **1975**, *47*, 98–114. [CrossRef]
81. Sivkov, D.V.; Petrova, O.V.; Nekipelov, S.V.; Vinogradov, A.S.; Skandakov, R.N.; Bakina, K.A.; Isaenko, S.I.; Ob'edkov, A.M.; Kaverin, B.S.; Vilkov, I.V.; et al. Quantitative Characterization of Oxygen-Containing Groups on the Surface of Carbon Materials: XPS and NEXAFS Study. *Appl. Sci.* **2022**, *12*, 7744. [CrossRef]
82. Ben Yaacov, A.; Ben David, R.; Grinter, D.C.; Held, G.; Eren, B. Identification of Adsorbed Species and Surface Chemical State on Ag(111) in the Presence of Ethylene and Oxygen Studied with Infrared and X-ray Spectroscopies. *Physchem* **2021**, *1*, 259–271. [CrossRef]
83. Pallavolu, M.R.; Kumar, Y.A.; Nallapureddy, R.R.; Goli, H.R.; Banerjee, A.N.; Joo, S.W. In-situ design of porous vanadium nitride@carbon nanobelts: A promising material for high-performance asymmetric supercapacitors. *Appl. Surf. Sci.* **2022**, *575*, 151734. [CrossRef]
84. Eguchi, K.; Nakagawa, T.; Takagi, Y.; Yokoyama, T. Direct Synthesis of Vanadium Phthalocyanine and Its Electronic and Magnetic States in Monolayers and Multilayers on Ag(111). *J. Phys. Chem. C* **2015**, *119*, 9805–9815. [CrossRef]
85. Osonkie, A.; Lee, V.; Chukwunenye, P.; Cundari, T.; Kelber, J. Plasma modification of vanadium oxynitride surfaces: Characterization by in situ XPS experiments and DFT calculations. *J. Chem. Phys.* **2020**, *153*, 144709. [CrossRef]

86. Liu, Y.; Liu, L.; Kong, L.; Kang, L.; Ran, F. Supercapacitor Electrode Based on Nano-Vanadium Nitride Incorporated on Porous Carbon Nanospheres Derived from Ionic Amphiphilic Block Copolymers & Vanadium-Contained Ion Assembly Systems. *Electrochim. Acta* **2016**, *211*, 469–477.
87. Klofta, T.J.; Danziger, J.; Lee, P.; Pankow, J.; Nebesny, K.W.; Armstrong, N.R. Photoelectrochemical and spectroscopic characterization of thin films of titanyl phthalocyanine: Comparisons with vanadyl phthalocyanine. *J. Phys. Chem.* **1987**, *91*, 5646–5651. [CrossRef]